Available online at www.sciencedirect.com
SCIENCE DIRECT®
ELSEVIER
International Journal of Solids and Structures 43 (2006) 3087–3105
INTERNATIONAL JOURNAL OF SOLIDS and STRUCTURES
www.elsevier.com/locate/ijsolstr

Prediction of central bursting during axisymmetric cold extrusion of a metal alloy containing particles

Cahal McVeigh, Wing Kam Liu *

Department of Mechanical Engineering, The Technological Institute, Northwestern University, 2145 Sheridan Road, Evanston, IL 60208-3111, United States

Received 4 February 2005; received in revised form 5 May 2005
Available online 11 July 2005

Abstract

A simple cell model based damage dependent yield surface is used to model the effect of void nucleation and growth in an aluminum alloy during an axisymmetric cold extrusion process. Material parameters for characterization of the yield surface are determined through a physically consistent micromechanical cell modeling technique. The model can account for the behavior of a void containing a particle under severe compressive processing conditions. The formation of distinct, equally spaced, arrowhead shaped 'central burst' defects is observed during simulation of the extrusion process. Application of the model to a two-stage rolling process is also briefly illustrated. Formation of central bursts during extrusion and edge cracking during rolling is explained in terms of the hydrostatic stress distribution and the related void growth. The affects of material hardening, surface friction and die geometry are examined in the case of extrusion. Correlation is found between the simulations and analytical and experimental results, confirming the suitability of the constitutive model.

Keywords: Central burst; Void growth; Axisymmetric extrusion; HLC model

1. Introduction

The cold extrusion process involves forcing a billet of material through a die at room or slightly elevated temperatures, producing a continuous product of constant cross-section. Numerous metals are suitable for cold extrusion, including lead, tin, aluminum alloys, copper, titanium, molybdenum, vanadium, and steel. A wide variety of parts can be produced, including collapsible tubes, aluminium cans, cylinders and gear

* Corresponding author. Tel.: +1 847 491 7094; fax: +1 847 491 3915.
E-mail address: w-liu@northwestern.edu (W.K. Liu).

0020-7683/$ - see front matter © 2005 Elsevier Ltd. All rights reserved.
doi:10.1016/j.ijsolstr.2005.05.019

Nomenclature

$\varepsilon_{ij}, \sigma_{ij}$	average strain and stress in a cell
V_{cell}	cell volume
$\varepsilon_{ij}^{\text{micro}}$, $\sigma_{ij}^{\text{micro}}$	microstress and strain
u_j	material velocity components
n_i	unit normal to the cell surface
S	cell surface
x_j	spatial coordinates
$\dot{\varepsilon}_{\text{I}}^{\text{total}}$	total strain rate
$\dot{\varepsilon}_{\text{I}}^{\text{void}}$	strain rate due to void damage
$\dot{\varepsilon}_{\text{I}}^{\text{matrix}}$	strain rate due to matrix material
m_{20}	instability ratio
σ_{y}	matrix yield stress
f	void volume fraction
m_1	material constant
ϕ	plastic potential
α	pressure parameter
r_{f}	die exit radius
r_0	die initial radius
$\mathbf{A}^{\text{p}}, \mathbf{A}^{\text{e}}$	plastic, elastic part of $\mathbf{A}$
a, b	constants in m_{20}
T, T_0	temp–current, initial
σ_{y0}	initial matrix yield stress
$\bar{\varepsilon}^{\text{p}}$	accumulated plastic strain
ε_{y}	yield strain in 1-d
β	temperature parameter
χ	temp-plastic strain rate coefficient
ρ	ρ is the material density
C_p	specific heat capacity
B	nucleation parameter
f_{n}	volume fraction of particles
s_{n}	standard deviation of nucleation
ε_{n}	average nucleation strain
f^*	void coalescence function
R_{a}	% reduction in area
γ	die semi-cone angle
$\Delta\mathbf{A}$, $\dot{\mathbf{A}}$	incremental, rate change of $\mathbf{A}$
$A_{\text{m}}, A_{\text{eq}}$	volumetric, equivalent part of $\mathbf{A}$
$\mathbf{A}_{\text{I}}$	principal values of $\mathbf{A}$

blanks. Cold extruded parts do not suffer from oxidation and often have improved mechanical properties due to severe cold working, as long as the billet temperature remains below the re-crystallization temperature.

However, defects may occur in the form of surface cracking and 'internal chevron cracking' or 'central bursting'. A substantial body of work exists in the area of central bursting and various approaches have

been taken to develop failure criteria and die geometry design curves. It is generally accepted that four main parameters are responsible for the onset of central bursting: reduction in cross-sectional area, die semi-cone angle, friction between the die and the billet and material hardening behavior.

Before efficient computational methods were at the disposal of researchers, Avitzur (1968) developed an analytical method for predicting the occurrence of central bursting in non-strain hardening materials during extrusion. This approach involves calculating the force required to extrude a cracked and an uncracked sample of material. If the driving force for the cracked sample is less than for the uncracked sample, central bursting will occur. This approach was extended by Zimerman and Avitzur (1970) to account for strain hardening; however it does not address the underlying micromechanics of the central bursting failure phenomena.

Attempts have also been made to use a Cockroft and Latham (1968) type energy criterion, notably by Ko and Kim (2000) and Liu and Chung (1990). As with most energy criteria no direct coupling between the damage criteria and the subsequent deformation is included in the model i.e. there is no damage effect on deformation. Other criteria involving the mean hydrostatic stress are used by Choi et al. (1997) and Siram and Van Tyne (2002), however again there is no link between damage and deformation.

As far back as 1952, Tanaka found that certain die geometries caused inhomogeneous deformation across the billet during extrusion. This gave rise to a tensile region on the billet center line which led to local failure, in certain cases. Tanaka (1952) proposed that fracture in this tensile region is caused by *interfacial decohesion of constituent particles leading to voids and ductile fracture*. This is consistent with experimental findings which date from 1930 when Remmers (1930) showed high porosity levels along the center line of damaged extrudates.

Aravas (1986) concluded that the mechanism which causes central bursting is similar to that which is responsible for rupture during uniaxial tension and ductile failure ahead of a crack. A Gurson (1977) type model was used to model the nucleation, growth and coalescence of voids during deformation within the die. All of the particles were assumed to nucleate at the initial yield strain due to interfacial debonding between the second phase particles and the matrix material. These voids could then grow, if in a region of tensile hydrostatic stress. The voids had no effect in compression and were effectively ignored. The work done by Aravas (1986) was a first attempt at modeling the onset of central bursting in a physically consistent manner, using a void damage model. More recently, Lim and Dunne (1996) have examined the central bursting phenomena during extrusion of reinforced metal matrix composite materials. They used a system of damage constitutive equations which incorporated void nucleation and growth. Central bursting is assumed to occur at a critical value of void volume fraction. This critical value is not suitable for use as a surface damage criterion within the same model.

The ultimate objective is to be able to design materials which are less susceptible to defects such as central bursting. This can be achieved by developing a material model which accurately replicates the microstructural behavior during large deformation processing. The goal of the present research is to develop a simple continuum level material model which can predict central bursting and give an insight into the causes of surface damage during axisymmetric extrusion of a typical particle containing metal alloy.

The most popular void damage model currently used is the well known Gurson, Tvergaard, Needleman (GTN) model (Tvergaard and Needleman, 1984) which requires three arbitrary parameters. These constants are added to improve the performance of the GTN model, without rigorous physical reasons for doing so. In this paper we use the Hao et al. (2000) (HLC) damage model. The HLC model can simulate the effect of void nucleation, growth and coalescence on the yield surface of a material. The model is extended here to more accurately account for the behavior of voids in compression, which is the prevalent stress state during an extrusion process. The HLC model used in this paper requires only one parameter, which is derived in a physically consistent manner, via a micromechanical cell modeling technique.

The HLC damage model is briefly explained and the internal variables are described in Section 2. The use of the model is illustrated with a simple tension test simulation in Section 3 and some compressive

considerations are highlighted. This is followed by a discussion of the material behavior during extrusion in Section 4. Further results are given in Sections 5 and 7. Conclusions are then made.

2. Material model development

The HLC (Hao et al., 2000) model uses a damage dependent yield surface based on a micromechanical cell modeling technique. It is similar in form to the Gurson (1977) potential and reduces to that potential in certain cases. Only one physically based material parameter, m_{20}, is required to describe the material behavior with the HLC potential. m_{20} is a strain based ratio which represents the instability failure of the micromechanical system. This parameter is a function of the stress triaxiality and the void volume fraction. A form for this parameter is derived using only the known elasto-plastic behavior of the matrix material through the cell modeling process described in Sections 2.1–2.3. The full development is in the paper by Hao et al. (2000).

2.1. Cell modeling

The cell modeling technique is useful because statistical averaging of the cell's constitutive behavior over a large number of 'unit cells' can effectively represent the macroscale behavior. It is possible to define an average stress and strain for a unit cell, such as that shown in Fig. 1a, by averaging the 'micro' stress and strain over the cell volume and applying the divergence theorem. Expressions for the resulting average strain and stress associated with a unit cell are given as

$$\varepsilon_{ij} = \frac{1}{V_{\text{cell}}} \int_V \varepsilon_{ij}^{\text{micro}} \, \mathrm{d}V = \frac{1}{2V_{\text{cell}}} \int_S \left(u_j n_i + u_i n_j\right) \mathrm{d}S \tag{2.1}$$

$$\sigma_{ij} = \frac{1}{V_{\text{cell}}} \int_V \sigma_{ij}^{\text{micro}} \, \mathrm{d}V = \frac{1}{2V_{\text{cell}}} \int_S \sigma_{ik}^{\text{micro}} n_k x_j \, \mathrm{d}S \tag{2.2}$$

We consider the maximum principal components of strain in a cell like that shown in Fig. 1b. We decompose the total strain rate, $\dot{\varepsilon}_{\text{I}}^{\text{total}}$, into the strain rate caused by void damage, $\dot{\varepsilon}_{\text{I}}^{\text{void}}$, and deformation of the matrix material without damage, $\dot{\varepsilon}_{\text{I}}^{\text{matrix}}$ as

$$\dot{\varepsilon}_{\text{I}}^{\text{total}} = \dot{\varepsilon}_{\text{I}}^{\text{void}} + \dot{\varepsilon}_{\text{I}}^{\text{matrix}} \tag{2.3}$$

2.2. Instability failure criteria

During deformation of a unit cell, an instability point will be reached at which the deformation becomes unstable and the rate of softening becomes greater than the rate of hardening. From experiments it can be

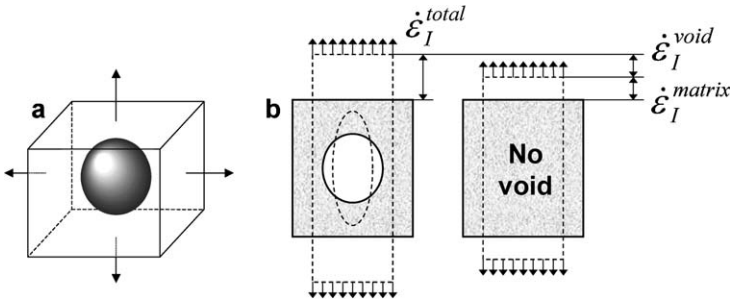

Fig. 1. (a) A typical cell model with a central void. (b) The additive behavior of strain rate due to voiding and strain rate in the matrix.

seen that during stable deformation, before the instability point, the ratio of $\dot{\varepsilon}_{\mathrm{I}}^{\mathrm{void}}$ to $\dot{\varepsilon}_{\mathrm{I}}^{\mathrm{matrix}}$ is approximately constant. However after the instability point the ratio increases rapidly indicating that the total strain rate is now mainly controlled by the strain rate due to void damage, $\dot{\varepsilon}_{\mathrm{I}}^{\mathrm{void}}$. Hao et al. (2000) recognized that the ratio of $\dot{\varepsilon}_{\mathrm{I}}^{\mathrm{void}}$ to $\dot{\varepsilon}_{\mathrm{I}}^{\mathrm{matrix}}$ at the instability point could be used as a failure criterion. The ratio at the instability point is named m_{20}, and with reference to Fig. 2a and b it can be written as (Hao et al., 2000):

$$m_{20} = \frac{\dot{\varepsilon}_{\mathrm{I}}^{\mathrm{void}}}{\dot{\varepsilon}_{\mathrm{I}}^{\mathrm{matrix}}} \approx \frac{\Delta\varepsilon_{\mathrm{I}}^{\mathrm{void}}}{\Delta\varepsilon_{\mathrm{I}}^{\mathrm{matrix}}} \quad \text{when} \quad \frac{\mathrm{d}\sigma_{\mathrm{I}}}{\mathrm{d}\varepsilon_{\mathrm{I}}^{\mathrm{matrix}}} = 0 \tag{2.4}$$

After some simple algebra and making use of work done by Rice and Tracy (1969), we can derive the relationship between the void volume fraction and the stress triaxiality at the instability point (Hao et al., 2000). See Appendix A for derivation of Eq. (2.5).

$$1 = \left(1 + \frac{1}{m_{20}}\right) f m_1 \exp\left(\frac{3\sigma_{\mathrm{m}}}{2\sigma_{\mathrm{y}}}\right) \tag{2.5}$$

A plastic potential incorporating the effect of void damage takes the form (Rousselier, 1981)

$$\phi = \phi_{\mathrm{matrix}}\left(\frac{\sigma_{\mathrm{eq}}}{\sigma_{\mathrm{y}}}, \frac{\sigma_{\mathrm{m}}}{\sigma_{\mathrm{y}}}\right) + \phi_{\mathrm{damage}}\left(\frac{\sigma_{\mathrm{m}}}{\sigma_{\mathrm{y}}}\right) \tag{2.6}$$

We can use Eq. (2.5) as the damage part of this plastic potential—it is equal to unity when plastic instability failure occurs due to voiding, and equal to zero when there are no voids (when $f = 0$). During yielding the material will be subject to high values of pressure in some areas and hydrostatic tension in others. The hydrostatic stress state will play an important role in influencing the material's yield behavior. To account for this pressure dependency it is common to use a Drucker–Prager (DP) type yield criterion for porous materials to represent the matrix behavior (Belytschko et al., 2000). In Eq. (2.6) we have $\phi_{\mathrm{matrix}} = \phi_{\mathrm{DP}}$ where

$$\phi_{\mathrm{DP}} = \left(\frac{\sigma_{\mathrm{eq}}}{\sigma_{\mathrm{y}}}\right)^2 + \alpha\frac{\sigma_{\mathrm{m}}}{\sigma_{\mathrm{y}}} - 1 \tag{2.7}$$

The resulting form for the potential, using the instability criteria of Hao et al. (2000) and a Drucker–Prager potential for the matrix material, is given as

$$\phi_{\mathrm{DP\text{–}HLC}} = \left(\frac{\sigma_{\mathrm{eq}}}{\sigma_{\mathrm{y}}}\right)^2 + \alpha\frac{\sigma_{\mathrm{m}}}{\sigma_{\mathrm{y}}} + \left(1 + \frac{1}{m_{20}}\right) f m_1 \exp\left(\frac{3\sigma_{\mathrm{m}}}{2\sigma_{\mathrm{y}}}\right) - 1 \tag{2.8}$$

The pressure parameter, α, is independent of void volume fraction, f, and stress triaxiality, $\frac{\sigma_{\mathrm{m}}}{\sigma_{\mathrm{eq}}}$. A small value is generally used for metals (Hao et al., 2004). Here a value of 0.05 is used.

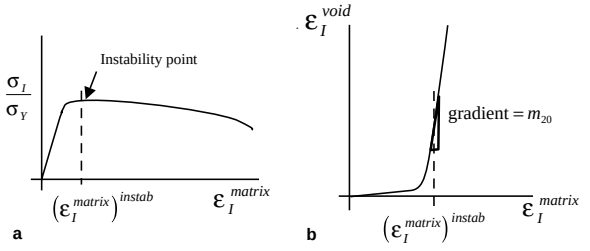

Fig. 2. (a) The instability deformation behavior of a unit cell. (b) The evaluation procedure for m_{20}.

2.3. Computation of material parameters by cell modeling

An expression for m_{20} is required to complete the potential. m_{20} depends on the void volume fraction, the average orientation and geometry of voids, stress state and matrix properties. These inputs can all be controlled in a cell model, making it an appropriate method for computing m_{20}. The instability behavior and hence the m_{20} parameter will depend on the stress triaxiality and the void volume fraction. From analysis of cell modeling results, m_{20} will take the form:

$$m_{20}\left(f,\frac{\sigma_{\mathrm{m}}}{\sigma_{\mathrm{y}}}\right)=a(f)\exp\left(b(f)\left(\frac{3\sigma_{\mathrm{m}}}{2\sigma_{\mathrm{eq}}}\right)\right) \tag{2.9}$$

Only the parameters 'a' and 'b' are required to complete the plastic potential. A prescribed displacement boundary condition is applied to a cell with a certain void volume fraction and the same cell with a zero void volume fraction. By using the averaging technique described by Eqs. (2.1) and (2.2) it is possible to create a plot of the average maximum principal stress, σ_{I}, versus the matrix strain, $\varepsilon_{\mathrm{I}}^{\mathrm{matrix}}$. The matrix strain corresponding to the maximum principal stress (the instability point) is then found.

Here it is called $\left(\varepsilon_{\mathrm{I}}^{\mathrm{matrix}}\right)^{\mathrm{instab}}$ as shown on Fig. 2a. A plot of the average strain in the matrix material, $\varepsilon_{\mathrm{I}}^{\mathrm{matrix}}$, versus the average strain due to void damage, $\varepsilon_{\mathrm{I}}^{\mathrm{void}}$, can also be produced; see Fig. 2b. Recalling Eq. (2.4) ($m_{20}=\frac{\dot{\varepsilon}_{\mathrm{I}}^{\mathrm{void}}}{\dot{\varepsilon}_{\mathrm{I}}^{\mathrm{matrix}}}\approx\frac{\Delta\varepsilon_{\mathrm{I}}^{\mathrm{void}}}{\Delta\varepsilon_{\mathrm{I}}^{\mathrm{matrix}}}$) and with reference to Fig. 2b, the slope of the $\varepsilon_{\mathrm{I}}^{\mathrm{matrix}}$ versus $\varepsilon_{\mathrm{I}}^{\mathrm{void}}$ curve at the instability value of matrix strain, $\left(\varepsilon_{\mathrm{I}}^{\mathrm{matrix}}\right)^{\mathrm{instab}}$, is the resulting m_{20} value. This value is unique to the void volume fraction and stress triaxiality combination used in that cell model. By varying the boundary conditions (Fig. 3a) and hence the triaxiality, whilst maintaining the same void volume fraction, we can plot the relationship between m_{20} and the triaxiality in Fig. 3b. From Fig. 3b it is obvious where the assumed exponential form for Eq. (2.9) originated. The procedure can be repeated for different void volume fractions. This produces the different curves shown in Fig. 3b. From these curves it is found that a linear relationship exists between 'a' and the void volume fraction, f. The parameter 'b' is found to be a constant. In the paper by Hao et al. (2000), the values of 'a' and 'b' are calculated. These values are used in the current paper. They are:

$$\begin{aligned} a &= 1.109-2.323f \\ b &= 0.352 \end{aligned} \tag{2.10}$$

2.4. Matrix flow stress

When examining a material with voids, it is important to distinguish between properties which are related to the matrix and to the macroscopic scale. Matrix properties are those which apply to the matrix

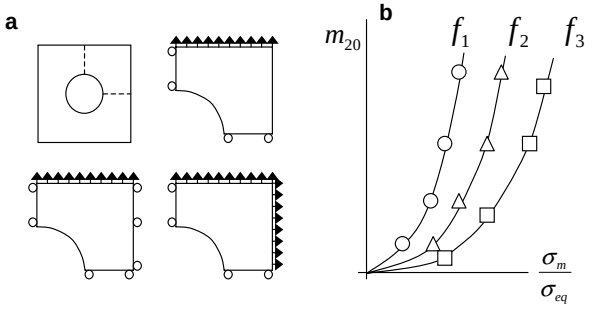

Fig. 3. (a) Different possible boundary conditions for the unit cell. (b) The variation of m_{20} for different void volume fractions.

Fig. 4. The difference between the properties associated with the matrix and macroscopic properties.

material only, whereas macroscopic properties apply to the overall material including voids as shown in Fig. 4.

The matrix flow stress of an aluminum alloy can be simulated using a Ludwik type flow law with temperature softening:

$$\sigma_y = \sigma_{y0}\left(1 + \frac{\bar{\varepsilon}^p}{\varepsilon_y}\right)^n (1 - \beta(T - T_0)) \tag{2.11}$$

Provided the strain hardening exponent is appropriately selected, the experimental stress–strain behavior can be well represented by this yield function. A temperature softening effect is incorporated. However it becomes important only at large plastic strains.

2.5. Evolution of internal state variables

The relationship between the matrix effective plastic strain and macroscopic stress and plastic strain can be specified by the equivalence of plastic work (Belytschko et al., 2000)

$$\underbrace{\boldsymbol{\sigma} : \Delta\boldsymbol{\varepsilon}^p}_{\text{work(macroscopic)}} = \underbrace{(1-f)\sigma_y \Delta\bar{\varepsilon}^p}_{\text{work(matrix)}} \tag{2.12}$$

Decomposing these tensors into their equivalent and hydrostatic/volumetric parts, we get an expression for the increment in matrix effective plastic strain:

$$\Delta\bar{\varepsilon}^p = \frac{\sigma_m \Delta\varepsilon_m^p + \sigma_{eq}\Delta\varepsilon_{eq}^p}{(1-f)\sigma_y} \tag{2.13}$$

We assume that temperature and plastic deformation are related by an adiabatic law, i.e. plastic dissipation is transformed to temperature increase.

$$\dot{T} = \frac{\chi\sigma_y}{\rho C_p}\dot{\bar{\varepsilon}}^p \tag{2.14}$$

where $\dot{T}$ is the rate of temperature increase, ρ is the material density, C_p is the specific heat capacity and χ is the temperature–plastic strain rate coefficient. Transforming this to the incremental form and substituting for the increment in matrix equivalent plastic strain from Eq. (2.13), we get:

$$\Delta T = \frac{\chi\sigma_y}{\rho C_p}\frac{\sigma_m \Delta\varepsilon_m^p + \sigma_{eq}\Delta\varepsilon_{eq}^p}{(1-f)\sigma_y} \tag{2.15}$$

Evolution of void volume fraction is driven by the growth of existing voids and nucleation of new voids, thus:

$$\Delta f = \Delta f_{\text{growth}} + \Delta f_{\text{nucleation}} \tag{2.16}$$

Void growth can be expressed by volumetric expansion in the matrix:

$$\Delta f_{\text{growth}} = (1-f)\Delta\boldsymbol{\varepsilon}^p : \mathbf{I} = (1-f)\Delta\varepsilon_m^p \tag{2.17}$$

We can consider plastic strain controlled nucleation such that void nucleation can be written as

$$\Delta f_{\text{nucleation}} = B\Delta\bar{\varepsilon}^{\text{p}} \tag{2.18}$$

B is chosen such that the nucleation strain follows a normal distribution (Chu and Needleman, 1980)

$$B = \frac{f_{\text{n}}}{s_{\text{n}}\sqrt{2\pi}} \exp\left[-\frac{1}{2}\left(\frac{\bar{\varepsilon}^{\text{p}} - \varepsilon_{\text{n}}}{s_{\text{n}}}\right)^2\right] \tag{2.19}$$

The total increment in void volume fraction can be given as

$$\Delta f = (1-f)\Delta\varepsilon_{\text{m}}^{\text{p}} + B\Delta\bar{\varepsilon}^{\text{p}} \tag{2.20}$$

The model can be summarized as

$$\phi_{\text{DP-HLC}} = \left(\frac{\sigma_{\text{eq}}}{\sigma_{\text{y}}}\right)^2 + \alpha\frac{\sigma_{\text{m}}}{\sigma_{\text{y}}} + \left(1 + \frac{1}{m_{20}}\right) f m_1 \exp\left(\frac{3\sigma_{\text{m}}}{2\sigma_{\text{y}}}\right) - 1 \tag{2.21}$$

where

$$m_1 = 3k, \quad k = 0.283, \quad \alpha = 0.05 \tag{2.22}$$

and

$$m_{20} = (1.109 - 2.323f)\exp\left(0.352\left(\frac{3\sigma_{\text{m}}}{2\sigma_{\text{eq}}}\right)\right) \tag{2.23}$$

3. Tensile behavior and compressive considerations

3.1. Tensile failure

In tension, the model given by Eqs. (2.11)–(2.23) is capable of simulating the deformation behavior of a metal alloy up to and including the point of failure by simulating the effects of void nucleation, growth and coalescence. However, some manipulation of the model is required for it to be effectively used in an extrusion problem, due to the presence of regions of high compressive stress. The final model is summarized in Fig. 6.

Fig. 5 shows a simulated stress–strain curve for an alloy, using the model described in this paper. The model can closely replicate the experimentally observed material behavior. As the strain reaches the average strain for void nucleation, ε_{n}, high levels of void nucleation occur. These voids are free to expand in the tensile stress state, leading to a rapid increase in void volume fraction. The void volume fraction has a large effect on the yield surface, and causes the steep failure region in Fig. 5. This is not possible to obtain using a Gurson model.

3.2. Compressive considerations

We now consider the influence of void behavior in compression on the yield surface.

3.2.1. Nucleation

Due to the complex microstructure of engineering metals, certain simplifying assumptions have been made in deriving this material model. The particles are assumed to be spherical, uniformly distributed

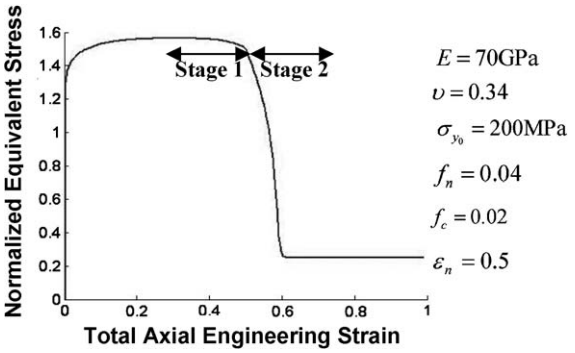

Fig. 5. The simulated stress strain curves for an alloy, using a 1-d uniaxial stress system. Stage 1 corresponds to void nucleation and growth. Stage 2 represents void coalescence and total failure at a material point.

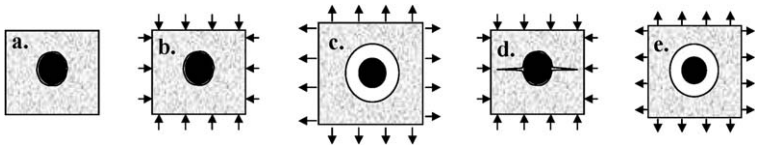

Fig. 6. The influence of the second phase particle on void damage.

and weakly bonded to the matrix. These assumptions allow us to ignore the complex stress state which would exist around a large particle as it debonds with the matrix. Instead, we can assume that all of the particles will undergo complete interfacial decohesion with the matrix immediately when the initial yield criterion is met in the surrounding matrix material, Fig. 6a. In the current model the initial yield criterion is the Drucker–Prager criterion, Eq. (2.7). With reference to Eq. (2.19), this is equivalent to having a strain controlled nucleation process, with the average nucleation strain (ε_n) and standard deviation of void nucleation (s_n) of zero. This is consistent with the work of Green and Knot (1976) who found that voids nucleate at inclusions at strains very close to the yield strain.

3.2.2. Void contraction in compression

Once interfacial decohesion occurs the particle effectively behaves as a void. We assume that in compression, any nucleated or partially grown voids will immediately collapse against the particle they nucleated at. The damage part of the potential is zero and the material will behave as if *fully dense*, with an *effective* void volume fraction of zero.

However, Fig. 7a and b reveal that the damage part of both the GTN and HLC potentials will have an influence on the yield surface even when the stress state is compressive. In particular, the symmetric GTN model, Fig. 7a, predicts a substantial void damage effect on the yield surface during compression. In the model used here, for compression, the potential reduces to a Drucker–Prager type law (Eq. (2.7)).

If the stress state becomes tensile, as is the case when central bursting occurs, the voids immediately re-open to there pre-compression size. Lim and Dunne (1996) followed a similar approach, assuming a constant void volume fraction in compression. This ensures that void damage in a material cannot be undone by compressive stresses. The voids are again able to grow and coalesce, Fig. 6c. The effect of the voids on the yield surface becomes important and the full potential ($\phi_{\mathrm{DP-HLC}}$)is used, Eqs. (2.11)–(2.13).

In essence, the presence of voids is a necessary, but not sufficient condition for softening—the stress state must also be tensile.

This is summarized in Fig. 6 as follows:

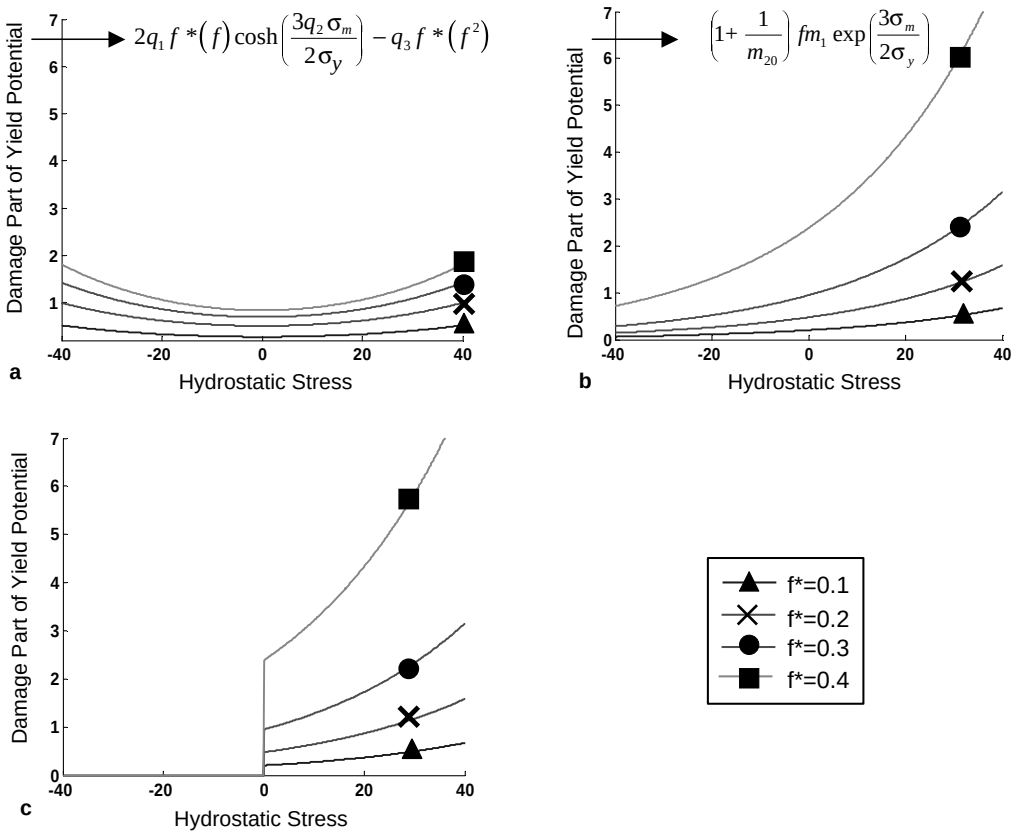

Fig. 7. (a) The damage part of the GTN model versus hydrostatic stress for different void volume fractions. (b) The damage part of the HLC model versus hydrostatic stress for different void volume fractions. (c) The form of the potential used in this model.

(a) Voids nucleate at the particle–matrix interface upon yielding. The particle behaves as a void.
(b) The nucleated voids have no effect if the stress state is initially compressive. The material behaves as if fully dense, with no voids. When $\sigma_m \leqslant 0, \phi = \phi_{DP}$.
(c) In tension the voids grow and softening occurs. When $\sigma_m > 0, \phi = \phi_{DP-HLC}$.
(d) In compression, the void cannot completely close due to the particle and it 'flattens out'. The material behaves as if fully dense. When $\sigma_m \leqslant 0, \phi = \phi_{DP}$.
(e) If the stress state returns to tension, the void returns to its pre-compression size (shown in 'c' i.e. before it 'flattened out'). When $\sigma_m > 0, \phi = \phi_{DP-HLC}$.

4. Implementation and billet behavior

4.1. Implementation in ABAQUS explicit

A Backward Euler scheme is used in the stress update algorithm to integrate the constitutive equation. This is used with the ABAQUS Explicit Solver through a VUMAT user material subroutine. The CAX4RT type element is used—a four-node bilinear axisymmetric quadrilateral element with reduced integration and hourglass control. Only half of the billet needs to be modeled for an axisymmetric problem. A symmetrical

boundary condition is applied to the center line of the billet. A displacement boundary condition is prescribed on the top face of the billet, at a constant rate. The sharp edges of the die are replaced by smooth curves of small radius, to avoid stress singularities in these areas. A sliding friction boundary condition is employed at the interface between the billet and the die. The process occurs at room temperature. Heat generation is assumed to occur due to plastic deformation, and heat generation due to friction on the surface is included through a coulomb friction law. The reduction in cross-sectional area is given by

$$R_a = 1 - \frac{r_f^2}{r_0^2} \tag{4.1}$$

where r_0 and r_f are the initial and final billet radii respectively. The die semi-cone angle is shown in Fig. 8.

4.2. Effective damage value

A typical plot of equivalent stress versus effective plastic strain (Fig. 5) shows the occurrence of severe damage and final failure of a material point as a massive drop in equivalent stress. At this point the 'Von Mises' part of the plastic potential will be almost equal to -1 as the equivalent stress approaches zero.

$$\left(\frac{\sigma_{eq}}{\sigma_y}\right)^2 - 1 \Rightarrow -1 \text{ as } \sigma_{eq} \Rightarrow 0 \quad \text{indicating total failure}$$

The remaining part of the potential, which consists of the Drucker–Prager term and the HLC damage term, will therefore become equal to 1 in order to maintain the consistency condition i.e. $\Phi_{DP-HLC} = 0$.

$$\alpha\frac{\sigma_m}{\sigma_y} + \left(1 + \frac{1}{m_{20}}\right) f m_1 \exp\left(\frac{3\sigma_m}{2\sigma_y}\right) \Rightarrow 1 \text{ as } \sigma_{eq} \Rightarrow 0 \quad \text{resulting in total failure}$$

We make use of this fact to illustrate the extent of damage in the billet as a contour of the above quantity, which we call the *effective damage value* or EDV. This ranges from 0, indicating no damage, to 1, indicating total failure of the material.

It is known that small reductions in area and large die semi-cone angles are primarily responsible for the occurrence of central bursting during cold extrusion. For this reason we begin with an angle of 48° and a reduction in area of 10% to gauge the quality of the results which can be achieved using the described model. The material properties are consistent with an aluminum alloy (6000 series) at room temperature i.e. a Young's modulus of 70 GPa and an initial yield strain of 290 MPa. The ability of the model to capture the central bursting phenomena is illustrated in Fig. 9, using a mesh of 320 (radial) × 720 (longitudinal) elements to represent half of the billet face. Fig. 9c shows a typical experimentally observed central bursting pattern for reference.

4.3. Billet material constitutive behavior

It is interesting to examine the constitutive behavior of two material points—one on the surface of the billet and another within a central burst region.

4.3.1. Surface: Point A on Fig. 9a

The material on the surface of the billet will undergo much higher levels of deformation than elsewhere. Damage along the surface depends on the die geometry and coefficient of friction. The material point

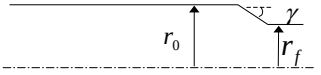

Fig. 8. Schematic of an axisymmetric extrusion setup.

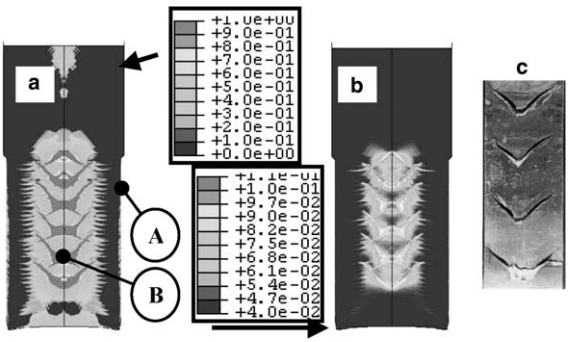

Fig. 9. (a) EDV contours in an extruded billet. (b) Void volume fraction contour. (c) Experimentally observed central bursting (Ko and Kim, 2000).

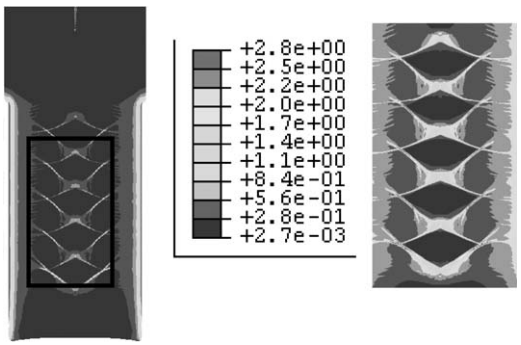

Fig. 10. Effective plastic strain contours in an extruded billet. Shear banding occurs in the high damage regions during simulation.

shown yields in compression, leading to interfacial debonding of the particles with the matrix (Fig. 11c). High values of plastic strain and compressive stress (Fig. 11b) occur along the surface of the billet due to contact with the die. The surface hydrostatic stress becomes tensile upon exit from the die. Significant and rapid void growth occurs (Fig. 11c), leading to a growth in the effective damage value (Fig. 11d), and a corresponding drop in equivalent stress (Fig. 11a).

4.3.2. Central burst: Point B on Fig. 9a

The material point initially yields in compression (Fig. 12a). The hydrostatic stress becomes tensile as the material enters the die (Fig. 12b). This results in void growth (Fig. 12c) and therefore an increase in the effective damage value (Fig. 12d). The increase in void volume fraction is accompanied by an increase in plastic strain due to softening. However the effective plastic strain remains small in comparison to the surface of the billet. The increase in effective damage value is accompanied by a rapid decrease in the equivalent stress and the material point loses its load carrying ability (Fig. 12a).

4.4. Prediction of distinct central bursts

Fig. 13 illustrates the contour of the EDV in the billet. The highest values occur along the center line where central bursting is observed experimentally. In reality, central bursting involves the formation of two traction

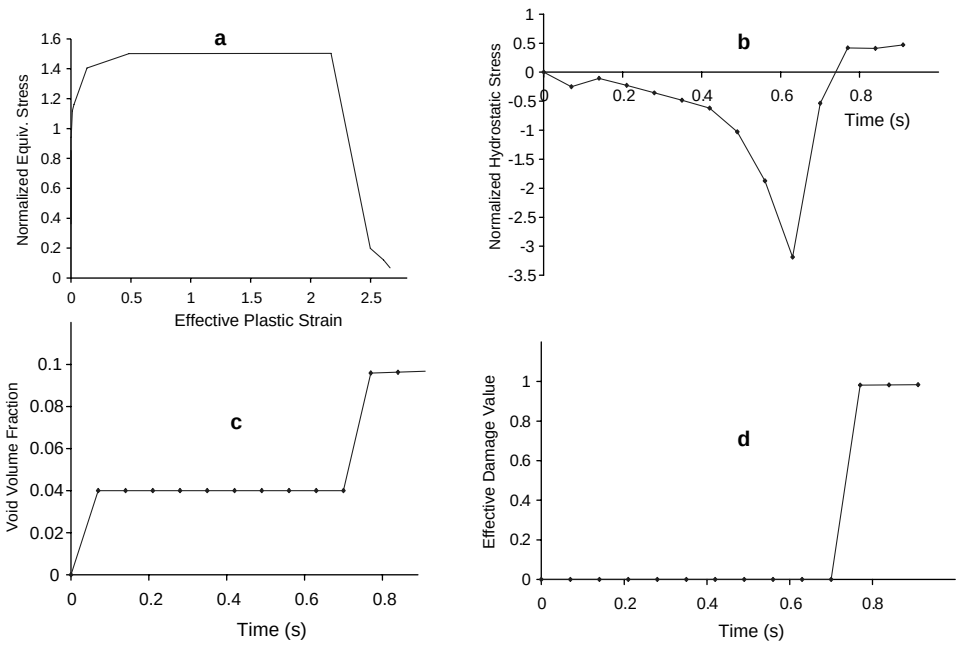

Fig. 11. Surface Point A: (a) Equivalent stress versus plastic strain, (b) hydrostatic stress versus time, (c) void volume fraction versus time and (d) effective damage value v time for a material point on the surface of the billet. Stresses normalized with the initial yield stress.

free surfaces (the crack faces), which leads to a stress relief zone around the cracks. Beyond the stress relief zone, plastic loading again occurs, leading to a periodic crack formation. The central burst defect makes a 45° angle with the extrusion direction i.e. along the plane of maximum shearing. The size of this zone is on the order of half a crack length. The simulated damage along the center of the billet can be explained as follows.

As the billet approaches and enters the die, inhomogeneous deformation takes place across the billet. Although the stress state is primarily compressive, certain combinations of die semi-cone angle and reduction in area will lead to a tensile region along the center line, within the die. Severe softening caused by void growth in the tensile region manifests itself as a rapid drop in the equivalent stress, which is accompanied by a high effective damage value (EDV). The region of high EDV in the simulation approximates to the traction free surfaces. The simulated material deforms in such a way as to minimize the energy necessary to push the billet through the die. This results in the shear banding observed in Fig. 10. The surrounding material undergoes relaxation, resulting in a stress relief zone. The level of hydrostatic stress within this zone is greatly reduced and is not capable of producing a significant level of void growth. Some distance away from the zone of high EDV, plastic loading again occurs and the conditions for void growth and high EDV are again met. This cycle continues and the material model reproduces the arrowhead shape of the central bursting defect. The spacing between 'cracks' remains on the order of one half of a crack length. The simulations indicate that the spacing is independent of friction and material hardening behavior.

5. Prediction of hardening, friction and geometry effects

It is now possible to examine the effect of strain hardening, friction and die geometry on the billet's failure behavior. A die with a semi-cone angle of 15° and reduction in area of 30% is used. This geometry is

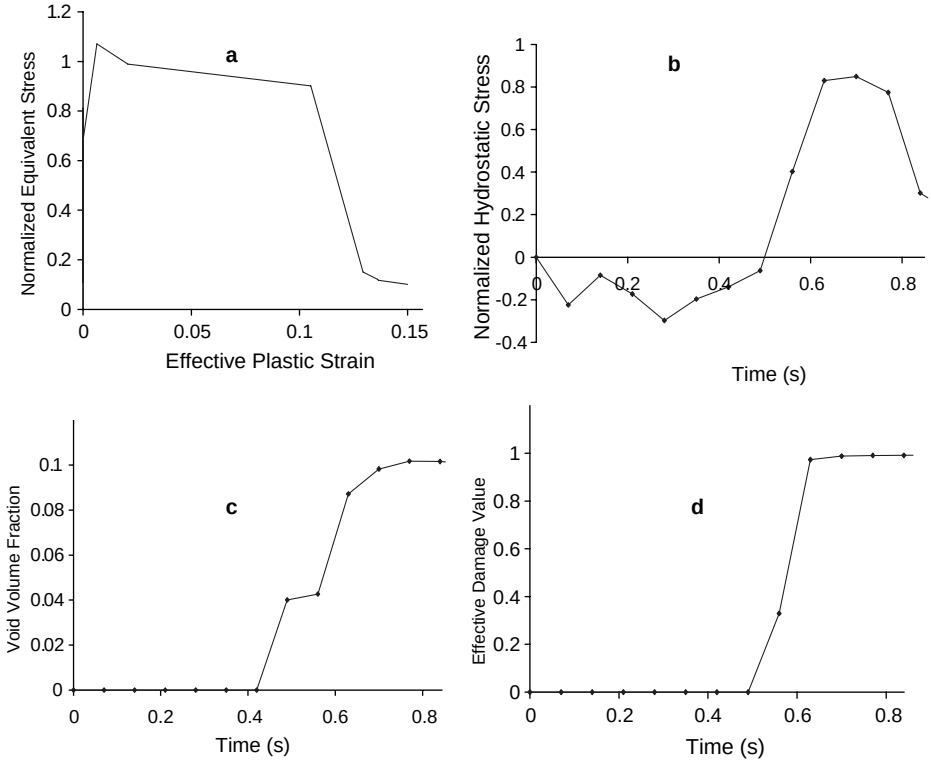

Fig. 12. Central burst Point B: (a) Equivalent stress versus plastic strain, (b) hydrostatic stress versus time, (c) void volume fraction versus time and (d) effective damage value v time for a material point on the center line. Stresses normalized with the initial yield stress.

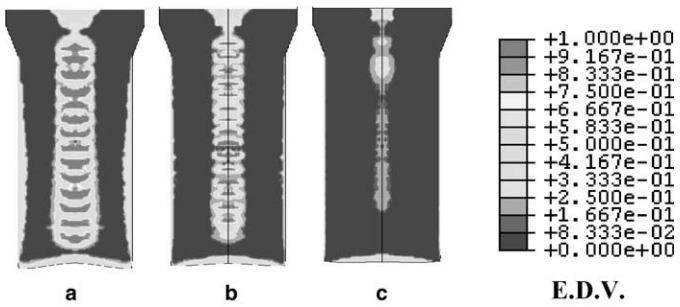

Fig. 13. Contours of EDV for 3 materials: (a) has a hardening exponent of 0.0, (b) 0.1 and (c) 0.25. The billet which undergoes the greatest hardening exhibits the lowest effective damage values along the surface and center line.

known to produce central bursting. A coarse mesh (40 radial × 120 longitudinal elements) has been used to represent the half billet for computational efficiency.

5.1. Strain hardening effect on damage

It is known that central bursting is more likely to occur in materials which undergo work hardening (Zimerman and Avitzur, 1970). In a non-work hardening metal, the material near the surface undergoes

high plastic strain, while the material near the center is more 'rigid' and is forced ahead, creating an inhomogeneous deformation field across the die. The deformation and hydrostatic stress field is much more homogeneous in a work hardening material. The flow stress of the matrix material used in the current model is subject to a plastic deformation dependant work hardening effect, determined by a hardening coefficient, n. The relationship is

$$\sigma = \sigma_{y0}\left(1 + \frac{\bar{\varepsilon}^{p}}{\varepsilon_{y0}}\right)^{n}(1 - \beta(T - T_0)) \tag{2.11}$$

It is clear from Fig. 13 that higher strain hardening leads to a decrease in the level and extent of the EDV along the center line and along the surface of the billet. The geometry used falls into the unacceptable zone for a *non-strain hardening material* ($n = 0.0$) according to Avitzur (1968), Fig. 16a.

5.2. Friction–defect relationship

Fig. 14 shows the predicted EDV contours for an extruded billet using values of 0.0, 0.1, 0.2 and 0.25 for the coefficient of friction. The level of damage along the center line significantly reduces as the friction coefficient increases. The maximum value of hydrostatic stress is reduced on the centerline as friction is increased, resulting in a more homogeneous deformation across the billet. This is consistent with the computational findings of Oh et al. (1979) and Lim and Dunne (1997), the experimental findings of Liu and Chung (1990) and the analytical treatment by Zimerman and Avitzur (1970).

Fig. 15a shows the relationship between central bursting and friction, as devised by Avitzur (1968). The interface between acceptable and unacceptable die geometry moves as friction is varied. The geometry used in Fig. 14 falls into the unsafe zone according to Fig. 15a, when a zero friction coefficient is used. From Fig. 14 it is clear that central bursting will not occur when a coefficient greater than 0.2 is used. This is consistent with Fig. 15a.

From Fig. 15b, the surface damage will increase with increasing friction. Aravas (1986) briefly mentions the residual porosities found near the surface of the billet and the tensile stresses which exist there upon exit from the die, but leaves the prediction of surface failure open for future research. Here we see that the EDV measure can be an effective way to predict damage levels throughout the billet.

5.3. Die geometry

Avitzur (1968) has used an upper bound analytical approach to develop the design curve in Fig. 16a and has verified the findings experimentally. We have simulated cold extrusions for a series of semi-cone angles and reductions in area. The resulting contour is shown in Fig. 16b. The Avitzur curve is superimposed on

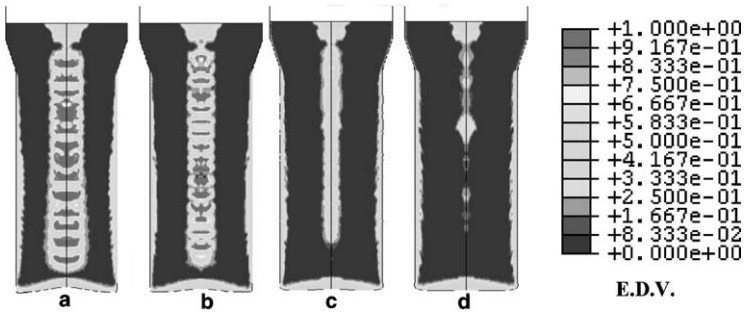

Fig. 14. Contours of EDV for 3 coefficients of friction between the billet and the die; (a) has a coefficient of 0.0, (b) 0.1, (c) 0.2 and (d) 0.25 (hardening exponent = 0.0).

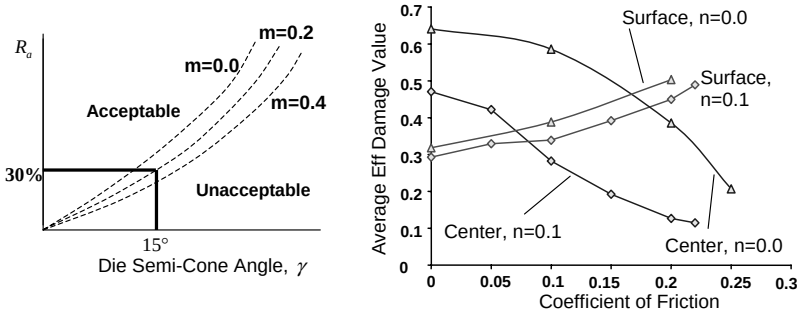

Fig. 15. (a) Schematic of the friction dependence design curve of Avitzur (1968), where m is the coefficient of friction. The highlighted curves demonstrate the friction effect illustrated in Fig. 14. (b) Effect of friction on the average effective damage value along the surface and center line of a billet. The center line average EDV decreases with increasing friction. The surface average EDV increases with friction.

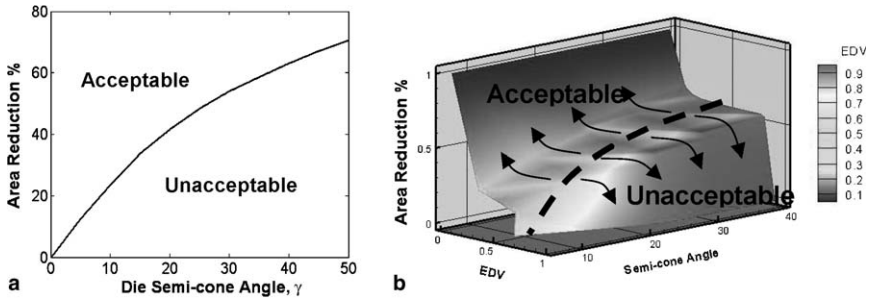

Fig. 16. (a) A reproduction of the analytical design curve of Avitzur (1968) for a non-strain hardening material with no friction (solid blue line). (b) A contour of EDV for different die geometries from the simulations. The Avitzur curve of (a) is superimposed (dashed line). It corresponds to a constant EDV of 0.5.

the contour. It is found to correspond very closely to a constant average EDV of 0.5. Therefore, an *average EDV* greater than 0.5 corresponds to the unacceptable region in the Avitzur curve.

6. Application to rolling—prediction of edge cracks

The mechanism responsible for central bursting is also the cause of undesirable edge cracking during cold rolling. Application of the model to cold rolling is briefly illustrated here. The model is capable of

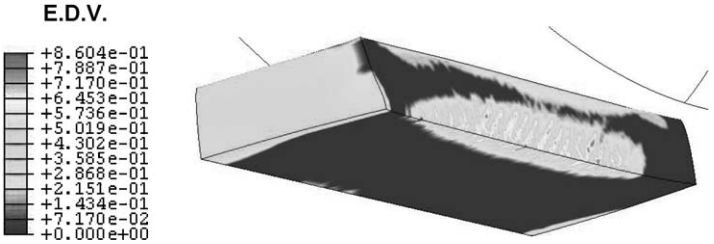

Fig. 17. A one quarter model of a rectangular section rolled bar. Discrete areas of high EDV form on the outer edges. These correspond to edge cracks.

capturing discrete edge cracks. Again, ABAQUS has been used, however now we use a 3-d setup. The effective damage value contour is shown in Fig. 17. Fig. 17 shows a one quarter model of a rectangular section bar. Discrete areas of high EDV form on the outer edges. These correspond to edge cracks.

7. Conclusion

A combined Drucker–Prager/HLC damage dependent yield surface along with a Ludwik type matrix flow stress law has been used to model the constitutive behavior of an aluminium alloy type metal during an axisymmetric cold forward extrusion process. The material parameters for the damage part of the potential are derived using a physically consistent micromechanics cell modeling technique.

The ability of the model to replicate the discrete arrowhead shaped central bursting defect has been demonstrated, indicating that the model has captured the main microscale mechanism which causes central bursting. The formation of distinct, periodic central bursts has been achieved.

This cell model based constitutive law has successfully been used to replicate the friction, hardening and geometry effects on the occurrence of central bursting and has also provided an insight into the occurrence of surface damage.

- It has been shown that increasing friction will increase the surface damage effect, whilst simultaneously there is a reduction in the observed central bursting.
- A strain hardening material will be less likely to suffer from central bursting during extrusion due to a more homogeneous deformation across the billet i.e. a lower value of hydrostatic stress along the center line.
- The model has successfully captured the well known dependency of central bursting on die geometry. The average *effective damage value* has been chosen to illustrate the predictive power of the material model. It has been shown that the average EDV will rise when the die semi-cone angle increases, or the reduction in area decreases.

It is not yet possible to comprehensively model the mechanics of the complex microstructure of a typical engineering metal during large deformation. Certain simplifying assumptions in terms of particle size, shape, distribution and behavior have been made. We have concentrated on capturing the behavior of small, weakly bonded particles such as the partially coherent ϑ' phase in an Al–Cu alloy. However, good correlation has been found between the simulations and analytical and experimental results, confirming the usefulness of the model as a simple tool for predicting an alloy's behavior during deformation. The model has also proved capable of predicting periodic edge cracks which form during cold rolling. For this model to be more effective as a material design tool, it is hoped that it can be developed to be more inclusive at the microstructural scale. Other important features which may be represented are particle size, spacing and orientation.

Acknowledgement

The authors gratefully acknowledge the support of the National Science Foundation and subsequently the Office of Naval Research. Cahal McVeigh gratefully acknowledges the support of the Northern Ireland Fund for Reconciliation and the assistance of Dr. Hongsheng Lu.

Appendix A

The strain rate can be decomposed into the strain rate due to the presence of a void, and the strain rate in the matrix.

$$\dot{\varepsilon}_{\mathrm{I}}^{\mathrm{total}} = \dot{\varepsilon}_{\mathrm{I}}^{\mathrm{void}} + \dot{\varepsilon}_{\mathrm{I}}^{\mathrm{matrix}} \tag{2.3}$$

The ratio of these quantities at the instability point can be written as (Hao et al., 2000)

$$m_{20} = \frac{\dot{\varepsilon}_{\mathrm{I}}^{\mathrm{void}}}{\dot{\varepsilon}_{\mathrm{I}}^{\mathrm{matrix}}} \approx \frac{\Delta\varepsilon_{\mathrm{I}}^{\mathrm{void}}}{\Delta\varepsilon_{\mathrm{I}}^{\mathrm{matrix}}} \quad \text{when} \quad \frac{\mathrm{d}\sigma_{\mathrm{I}}}{\mathrm{d}\varepsilon_{\mathrm{I}}^{\mathrm{matrix}}} = 0 \tag{2.4}$$

The void volume fraction, f, can be defined as

$$f = \frac{V_{\mathrm{void}}}{V_{\mathrm{matrix}} + V_{\mathrm{void}}} \tag{A.1}$$

where V_{void} is the volume of a void, and V_{matrix} is the volume of the matrix material in a representative cell. The volume of a spherical void is

$$V_{\mathrm{void}} = \frac{4}{3}\pi r^3 \tag{A.2}$$

where r is the void radius.

In a representative cell, the principal strain rate due to the void, $\dot{\varepsilon}_{\mathrm{I}}^{\mathrm{void}}$ can be approximated as

$$\dot{\varepsilon}_{\mathrm{I}}^{\mathrm{void}} \approx \frac{\mathrm{d}}{\mathrm{d}t}(f) \tag{A.3}$$

We can now expand (A.3) in terms of the volume of the void, V_{void} and matrix volume, V_{matrix}. It is pertinent to make the approximation

$$f = \frac{V_{\mathrm{void}}}{V_{\mathrm{void}} + V_{\mathrm{matrix}}} \approx \frac{V_{\mathrm{void}}}{V_{\mathrm{matrix}}} \tag{A.4}$$

This is true for $V_{\mathrm{matrix}} \gg V_{\mathrm{void}}$. Simplification of the algebra is substantial, allowing for the development of a closed form model. The evolution equations of Section 2.5 are consistent with (A.1). Had f been defined as $f = \frac{V_{\mathrm{void}}}{V_{\mathrm{matrix}}}$, approximation (A.3) would still hold because $V_{\mathrm{matrix}} \gg V_{\mathrm{void}}$ and the evolution equations would need to be redefined in terms of the new void volume fraction definition. Due to the relatively small void volume fractions considered, the change in simulated constitutive behavior is negligible.

Substituting for V_{void} from (A.2) into Eq. (A.3) yields an expression for the strain rate caused by void damage, $\dot{\varepsilon}_{\mathrm{I}}^{\mathrm{void}}$, in terms of the current void volume fraction, f, void radius, r and rate of change of void radius, $\dot{r}$:

$$\dot{\varepsilon}_{\mathrm{I}}^{\mathrm{void}} \approx \frac{\mathrm{d}}{\mathrm{d}t}\left(\frac{4/3\pi r^3}{V_{\mathrm{cell}}}\right) = 3\left(\frac{4/3\pi r^3}{V_{\mathrm{cell}}}\right)\frac{\dot{r}}{r} = 3f\frac{\dot{r}}{r} \tag{A.5}$$

Rice and Tracy (1969) proposed a void growth law of the form:

$$\frac{\dot{r}}{r} = k\dot{\varepsilon}_{\mathrm{I}}^{\mathrm{total}} \exp\left(\frac{3\sigma_{\mathrm{m}}}{2\sigma_{\mathrm{y}}}\right) \tag{A.6}$$

where $k = 0.283$, r is the void radius and σ_{m} is the hydrostatic stress. $\dot{\varepsilon}_{\mathrm{I}}^{\mathrm{total}}$ is the total principle strain rate. Substituting into (A.5) for $\frac{\dot{r}}{r}$ we get

$$\dot{\varepsilon}_{\mathrm{I}}^{\mathrm{void}} = 3f\frac{\dot{r}}{r} = fm_1\dot{\varepsilon}_{\mathrm{I}}^{\mathrm{total}} \exp\left(\frac{3\sigma_{\mathrm{m}}}{2\sigma_{\mathrm{y}}}\right) \tag{A.7}$$

Here $m_1 = 3k$. Recalling from (2.3) that the total strain rate can be decomposed as $\dot{\varepsilon}_{\mathrm{I}}^{\mathrm{total}} = \dot{\varepsilon}_{\mathrm{I}}^{\mathrm{void}} + \dot{\varepsilon}_{\mathrm{I}}^{\mathrm{matrix}}$ and substituting (2.4) into (2.3), at the instability (plastic collapse) point we get

$$\dot{\varepsilon}_{\mathrm{I}}^{\mathrm{total}} = \dot{\varepsilon}_{\mathrm{I}}^{\mathrm{void}} + \frac{1}{m_{20}}\dot{\varepsilon}_{\mathrm{I}}^{\mathrm{void}} \tag{A.8}$$

Substituting for the strain rate due to void damage, $\dot{\varepsilon}_{\mathrm{I}}^{\mathrm{void}}$ from (A.7), this becomes:

$$\dot{\varepsilon}_{\mathrm{I}}^{\mathrm{total}} = \left(1 + \frac{1}{m_{20}}\right) f m_1 \dot{\varepsilon}_{\mathrm{I}}^{\mathrm{total}} \exp\left(\frac{3\sigma_{\mathrm{m}}}{2\sigma_{\mathrm{y}}}\right) \tag{A.9}$$

Dividing (A.9) through by $\dot{\varepsilon}_{\mathrm{I}}^{\mathrm{total}}$ we get (Hao et al., 2000)

$$1 = \left(1 + \frac{1}{m_{20}}\right) f m_1 \exp\left(\frac{3\sigma_{\mathrm{m}}}{2\sigma_{\mathrm{y}}}\right) \tag{A.10}$$

References

Aravas, N., 1986. The analysis of void growth that leads to central bursts during extrusion. Journal of the Mechanics and Physics of Solids 34 (1), 55–79.

Avitzur, B., 1968. Analysis of central bursting in extrusion and wire drawing. Journal of Engineering for Industry 79, 79–91.

Belytschko, T., Liu, W.K., Moran, B., 2000. Nonlinear Finite Elements for Continua and Structures. John Wiley & Sons.

Chu, C.C., Needleman, A., 1980. Void nucleation effects in biaxially stretched sheets. Journal of Engineering and Materials Technology 102, 249–256.

Choi, S., Lee, Y., Oh, H., 1997. Ductile fracture in axisymmetric extrusion. Journal of Materials Processing Technology 74, 263–267.

Cockroft, M.G., Latham, D.J., 1968. Ductility and workability of metals. Journal of the Institute of Metals 96, 33–39.

Green, G., Knot, J.F., 1976. Initiation and propagation of ductile fracture in low strength steels. Journal of Engineering Materials and Technology 98, 37–46.

Gurson, A.L., 1977. Continuum theory of ductile rupture by void nucleation and growth: Part I—Yield criteria and flow rules for porous ductile material. Journal of Engineering Materials Technology 99, 2–15.

Hao, S., Liu, W.K., Chang, C.T., 2000. Computer implementation of damage models by finite element and meshfree methods. Computational Methods for Applied Mechanics and Engineering 187, 401–440.

Hao, S., Liu, W.K., Moran, B., Vernerey, F., Olson, G.B., 2004. Multi-scale constitutive model and computational framework for the design of ultra-high strength, high toughness steels. Computer Methods in Applied Mechanics and Engineering 193 (17–20), 1865–1908.

Ko, D., Kim, B., 2000. The prediction of central burst defects in extrusion and wire drawing. Journal of Materials Processing Technology 102, 19–24.

Lim, L.G., Dunne, F.P.E., 1996. Modelling central bursting in the extrusion of particulate reinforced metal matrix composite materials. International Journal of Machine Tools and Manufacture 37 (7), 901–915.

Lim, L.G., Dunne, F.P.E., 1997. Modelling void nucleation and growth in axisymmetric extrusion. Journal of Engineering Manufacture 211 (B4), 285–297.

Liu, T.S., Chung, N.L., 1990. Extrusion analysis and workability prediction using FE method. Computers and Structures 36 (2), 369–377.

Oh, S.I., Chen, C.C., Kobayashi, S., 1979. Ductile fracture in axisymmetric extrusion and drawing. Part 2: Workability in extrusion and drawing. Journal of Engineering for Industry 101, 23–44.

Remmers, W.E., 1930. Transactions of the AIME 89, 107.

Rousselier, G., 1981. Finite deformation constitutive relations including ductile fracture damage. In: Nemat-Nasser, S. (Ed.), Three dimensional constitutive relations and ductile fracture. pp. 331–355.

Rice, J.R., Tracy, D.M., 1969. On the ductile enlargement of voids in triaxial stress fields. Journal of the Mechanics and Physics of Solids 17 (1), 201–217.

Siram, S., Van Tyne, C.J., 2002. Criterion for prevention of central bursting in forward extrusions through spherical dies using the finite element method. Journal of Manufacturing Science and Engineering 124, 65–70.

Tanaka, H., 1952. Journal of the Japan Institute of Metals 16, 567.

Tvergaard, V., Needleman, A., 1984. Analysis of the cup cone fracture in a round tensile bar. Acta Metallurgica 32 (1), 157–169.

Zimerman, Z., Avitzur, B., 1970. Metal flow through canonical converging dies—a lower upper bound approach using generalized boundaries of the plastic zone. Journal of Engineering for Industry 92, 119–129.